

Strain-induced Weyl and Dirac states and direct-indirect gap transitions in group-V materials

Glenn Moynihan,^{1,*} Stefano Sanvito,¹ and David D. O'Regan¹

¹*School of Physics, CRANN and AMBER,
Trinity College Dublin, Dublin 2, Ireland*

(Dated: January 26, 2018)

Abstract

We perform comprehensive density-functional theory calculations on strained two-dimensional phosphorus (P), arsenic (As) and antimony (Sb) in the monolayer, bilayer, and bulk α -phase, from which we compute the key mechanical and electronic properties of these materials. Specifically, we compute their electronic band structures, band gaps, and charge-carrier effective masses, and identify the qualitative electronic and structural transitions that may occur. Moreover, we compute the elastic properties such as the Young's modulus Y ; shear modulus G ; bulk modulus \mathcal{B} ; and Poisson ratio ν and present their isotropic averages of as well as their dependence on the in-plane orientation, for which the relevant expressions are derived. We predict strain-induced Dirac states in the monolayers of As and Sb and the bilayers of P, As, and Sb, as well as the possible existence of Weyl states in the bulk phases of P and As. These phases are predicted to support charge velocities up to 10^6 ms^{-1} and, in some highly anisotropic cases, permit one-dimensional ballistic conductivity in the puckered direction. We also predict numerous band gap transitions for moderate in-plane stresses. Our results contribute to the mounting evidence for the utility of these materials, made possible by their broad range in tuneable properties, and facilitate the directed exploration of their potential application in next-generation electronics.

PACS numbers: 62.25.-g, 73.61.-r, 81.07.-b

* omuinneg@tcd.ie

I. BACKGROUND

Two-dimensional black phosphorus (BP), or *phosphorene*, is one of several predicted stable allotropes of few-layer phosphorus [1–4], and it has attracted considerable attention since its recent successful synthesis [5–9] that is now possible with liquid phase exfoliation [10, 11]. The excitement behind BP is driven by its growing list of technologically relevant anisotropic mechanical and electronic properties. The theoretically predicted properties include a tuneable band-gap [8, 12–17], a negative Poisson’s ratio [18], anisotropic conduction [19, 20], and linear dichroism [21, 22]. The properties that have been experimentally verified so far include a high hole-mobility between 300 – 1000 cm²/Vs [7, 8, 21, 23], considerable mechanical flexibility [24], and a layer-dependent band gap [22, 25, 26] ranging from 0.3 eV in bulk to 2.0 eV in the monolayer. The anisotropic crystal structure of BP is responsible for its unusual electro-mechanical properties, which are predicted to be strongly directional-dependent and highly responsive to mechanically strain [11, 19].

With this renewed interest in BP, focus has quickly turned to few-layer phases of the other pnictogens, namely arsenic [28] (As), antimony [29] (Sb), bismuth [30, 31] (Bi), and their alloys [32–36], which are attracting steadily increasing attention. Moreover, the search for a bulk counterpart to graphene, capable of supporting ballistic electron transport, has recently driven the search for new Weyl and Dirac semi-metals [37–47]. In spite of the difficulty in attaining Dirac points in two-dimensional materials [46, 47], the first experimental Dirac semi-metal in few-layer BP was observed by Kim *et al.* [48], while As [49], Sb [50–52], Bi [51], and P [51–54] are also predicted to be potential candidates. Indeed, many of the predicted strain-induced properties of these materials, such as direct-indirect band gap transitions [13, 28, 29, 55, 56], a negative Poisson’s ratio [18, 57], as well as electronic [2, 55, 58], structural [59], and topological [51, 60–62] transitions, are already spurring their incorporation in emergent technologies such as field-effect transistors [8, 20], gas-sensors [63, 64], optical switches [65, 66], solar-cells [34], next-generation batteries [67–69], reinforcing fillers [11, 70], and topological insulators [50, 51, 60–62].

In this work, our aim is to provide a comprehensive analysis of the monolayer, bilayer and bulk phases of orthorhombic P, As and Sb, in order to identify and compare the qualitative strain-related properties of each structure from a consistent set of calculations, thus treating each material on the same footing. Our findings provide new insights into their

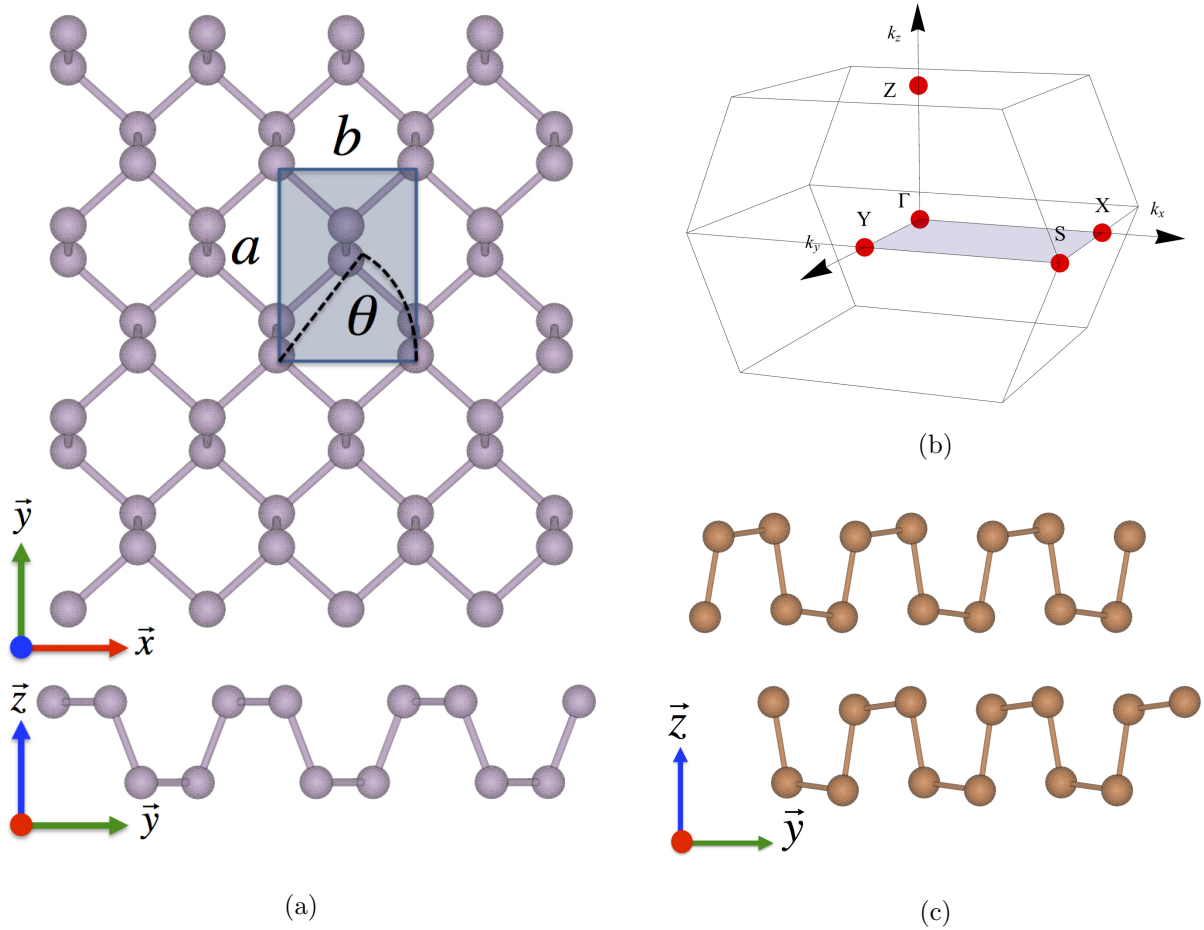


FIG. 1: (Color online) a) Top and side view of the 2D orthorhombic puckered structure (generated in VESTA [27]) with the primary vectors along the zigzag (\vec{x}) and puckered (\vec{y}) directions shown. The unit cell, given by the shaded region, is described by the lattice parameters a and b with the in-plane angle θ also defined. b) 3D Brillouin zone with high-symmetry points Γ , X , S , Y , and Z . c) Side-view of the buckled Sb state at $\varepsilon_{yy} = -4\%$ compressive strain.

electro-mechanical properties, especially regarding arsenic and antimony, which have been relatively unexplored to date. Specifically, we identify qualitative transitions in band gaps, effective masses, structure, and topology that occur at various strains, and compute the elastic properties that determine the required stresses to attain these electronic states.

We predict the existence of strain-induced Dirac states in monolayer As and Sb, bilayer P, As and Sb, as well as possible Weyl states in bulk P and As, at moderate stress values. Our findings show that all of the predicted Dirac and Weyl points are indeed linear, at

least in the $\Gamma - Y$ direction, i.e. the puckered direction. Thus, following the convention of terminology found in the Refs. [38, 48, 71], and other sources, we classify Dirac or Weyl states as those associated with regions of sustained linear dispersion in the band structure, at or near the Fermi level, in at least one direction. We predict these states to support ballistic conduction and are unaffected by the spin-orbit coupling (SOC). In particular, few-layer P and As exhibit a strong indication of anisotropic conduction, dominated by ballistic conductivity along $\Gamma - Y$.

The outline of this article is as follows: In Section II we review the details of our calculations and discuss the Voigt-Reuss-Hill averaging scheme used to compute the experimentally-relevant elastic properties. In Section III we present the results of our calculations including the lattice constants, strain dependence of electronic properties, in particular the potential Dirac and Weyl states identified, and computed elastic properties. We conclude in Section IV with a discussion of the implications of our key results.

II. METHODOLOGY

A. Calculation details

The calculations were performed with the QUANTUMESPRESSO package [72] using the Perdew-Burke-Ernzerhof (PBE) form of the generalized-gradient approximation (GGA) exchange-correlation functional [73]. An ultrasoft pseudopotential [74] from the SSSP Library [75] (with 5 valence electrons) was used to represent the core electrons. Non-SOC calculations were initially performed and those that exhibited potential Dirac or Weyl states were reassessed including non-perturbative SOC. In all calculations, van der Waals (vdW) interactions were incorporated using the B97-D empirical dispersion correction functional [76]. In order to achieve an energy convergence of at least 1 meV/atom and force convergence of at least 1.3×10^{-4} eV/ a_0 , we found it sufficient to use a common plane-wave energy cutoff of 1100 eV with ‘cold’ smearing [77] of 10^{-4} K for all elements. To achieve the same convergence, the Brillouin zone sampling for bulk systems was $15 \times 15 \times 15$, and $15 \times 15 \times 1$ for monolayers and bilayers. Uniaxial and shear strains between $\pm 5\%$ were applied in increments of 1% to the unit cell with internal relaxation subject to the same force convergence criterion as above. Electronic band structures were calculated along the high-symmetry

points of the Brillouin zone $\{\Gamma, X, S, Y, Z\}$ (Fig. 1b) for each value of in-plane strain (Figs. S1 - S9 in the [Supplemental Material](#)). For shear strains the Brillouin zone deforms into an asymmetric honeycomb, yet we continued to sample along the original path since the deformation up to 5% strain is negligible and the effective masses are all calculated at the Γ -point. We determine the Kohn-Sham band gap from the band structures and charge-carrier effective masses according to the nearly-free electron model $m_{ij}^* = \hbar^2 (\partial^2 E / \partial k_i \partial k_j)^{-1}$ using a cubic spline fit to 9 data points about the Γ -point. The charge velocities were similarly determined according to the dispersion relation $v = \hbar^{-1} dE(k)/dk$ from the linear fit to the Dirac or Weyl lines. The elements of the stiffness matrix C were derived from the gradients of the resultant stress-strain profiles $c_{ij} = \partial \sigma_i / \partial \varepsilon_j$, from which all elastic properties were derived. In practice, however, the computed stiffness tensors are not exactly symmetric due to numerical noise but we make them so by taking the average of C and its transpose C^T as the *effective* stiffness tensor. We begin our discussion with a brief overview of the the Voigt-Reuss-Hill scheme, which is a popular model used for computing effective isotropic elastic properties.

B. The Voigt-Reuss-Hill scheme

In order to effectively preserve, study and strain-engineer few-layer nano-structures, such as BP [78], graphene [79], or molybdenum disulfide [80] (MoS_2), the nano-flakes are typically deposited onto a suitable substrate. The cumulative contribution of dispersed nano-flakes distributed on or within a bulk medium results in the macroscopic elastic properties that are measured by experiments. The theoretical calculation of these elastic properties requires an appropriate mixture model (such as the rule-of-mixtures [11] (ROM) or the Halpin-Tsai [81] models) that require the (typically averaged) elastic properties of the interstitial nano-flakes.

In the theory of effective media, isotropic bulk properties are computed by averaging the stiffness tensor C over all possible rotated reference frames [82–84], as outlined in the Supplemental Material. The result is called the Voigt average [85, 86] and it gives isotropic averages for the bulk Young’s modulus Y_V , and shear modulus G_V , given in Eq. S7. The same scheme applied to the compliance tensor S results in the corresponding Reuss averages [87], Y_R and G_R , given in Eq. S9. The Voigt scheme assumes that the material undergoes constant strain and it returns over-estimated elastic constants. Conversely, the Reuss scheme assumes

constant stress and it tends to under-estimate the elastic constants. The Hill averages [88]

$$Y_H = \frac{Y_V + Y_R}{2}, \quad \text{and} \quad G_H = \frac{G_V + G_R}{2}, \quad (1)$$

from which the isotropic Poisson's ratio ν_H and bulk modulus \mathcal{B}_H are expressed as

$$\nu_H = \frac{Y_H}{2G_H} - 1, \quad \text{and} \quad \mathcal{B}_H = \frac{Y_H G_H}{3(3G_H - Y_H)}. \quad (2)$$

These are widely considered as reliable estimates of the actual physical values [84]. The Voigt-Reuss-Hill approach described above is used in the present work to determine the isotropic averages of the Young's, shear and bulk moduli, and the Poisson ratio of the bulk P, As, and Sb structures using the elements of the elastic tensors. Let us now discuss how the above approach may be adapted to derive the relevant equations for the specific case of two-dimensional materials.

C. In-plane Voigt-Reuss-Hill average

If the interstitial nano-flakes in a bulk medium form high-quality planar sediments [11, 89–95], the random orientation occurs instead in the plane of the flakes and we must calculate isotropic-averages *in-plane*. Due to the weak vdW bonds between layers, strains related to out-of-plane directions can be ignored resulting in the reduced-stiffness tensor (Eq. S3). In the Supplemental Material, we re-derive the angular dependence of the rotated tensor-elements $C_{ij}(\theta)$ and $S_{ij}(\theta)$ about the \vec{z} -axis (Eq. S6) as a function of the elements in the original reference frame, similar to the general Voigt-Reuss scheme. The angular-dependence of the in-plane elastic constants are then expressed as

$$\begin{aligned} Y_V(\theta) &= \frac{C_{11}^2 - C_{12}^2}{C_{11}}, & G_V(\theta) &= C_{66}, & \nu_V(\theta) &= \frac{C_{12}}{C_{11}}, \\ Y_R(\theta) &= \frac{1}{S_{11}}, & G_R(\theta) &= \frac{1}{S_{66}}, & \nu_R(\theta) &= -\frac{S_{12}}{S_{11}}, \end{aligned} \quad (3)$$

with the Hill-average taken as in Eq. 1. By integrating the elastic tensors $C_{ij}(\theta)$ and $S_{ij}(\theta)$ over 2π , the in-plane averages are then computed analogously.

III. RESULTS

A. Lattice Constants

The lattice constants a , b , c of the fully-relaxed structures are presented in Table I, where, in the monolayer and bilayer cases, we quote the layer thickness c' instead of the unit cell height c . Our computed lattice parameters compare well with other recent theoretically predicted values [28, 29, 51, 59, 96–99] and the available experimental data [100, 101]. For a

	a (Å)	b (Å)	c (Å)
P _{mono}	4.57	3.31	2.11
P _{bi}	4.51	3.31	7.34
P _{bulk}	4.43 (4.37 ^a)	3.32 (3.31 ^a)	10.47 (10.47 ^a)
As _{mono}	4.70	3.67	2.39
As _{bi}	4.64	3.69	7.86
As _{bulk}	4.56 (4.47 ^b)	3.71 (3.65 ^b)	10.94 (11.0 ^b)
Sb _{mono}	5.02	4.23	2.79
Sb _{bi}	4.88	4.26	8.83
Sb _{bulk}	4.73	4.29 (4.3 ^c)	12.09 (11.2 ^c)

^a Ref. [100]

^b Ref. [101]

^c Ref. [102]

TABLE I: Lattice parameters (Å) for monolayer, bilayer and bulk structures of P, As, Sb compared to experimental data [100–102] quoted in parentheses. For the monolayers and bilayers the layers thickness c' is given.

given element, we find that the lattice parameter along the puckered direction, ‘ a' ’, shortens as the number of layers increases, which agrees with observations in other studies. This is attributed to the increased vdW forces between layers, which leads to increased binding primarily in the softer puckered direction.

B. Electronic properties

All of the band structures pertaining to the following analysis are presented in Figs. S1 - S9 of the Supplemental Material. Where we identify possible Dirac or Weyl states, high resolution, three-dimensional band structures with SOC at representative strains are recalculated. To confirm the existence of linear-dispersion, we also plot lines along the surface of the Dirac and Weyl points at 0° , 30° , 60° and 90° with respect to the $\Gamma - X$ line. A representative sample of these results are presented in Figs. 5a - 5g, while the rest can be found in Figs. S10 - S13 of the Supplemental Material.

In general we find the band gap to be very responsive to uniaxial in-plane strain but significantly less so with respect to shear strain. We identify several direct-indirect band gap transitions as well as the opening and closing of band gaps, summarized in Table III. We find the charge-carrier effective masses vary approximately linearly with respect to the uniaxial strain in general but with notable exceptions that will be discussed. This section is divided into three parts discussing each of the species - P, As and Sb - for which we review the qualitative calculation results including band gap transitions, effective mass behavior and linearly-dispersive bands.

1. Phosphorus

As shown in Fig. 2a, our calculations reproduce the direct band gap of 0.88 eV at the Γ -point in the relaxed P monolayer, which falls within range of the reported gap between 0.7 eV (DFT-PBEsol [12]) and 1.0 eV (DFT-HSE06 [8]). On the other hand, quasi-particle calculations predict a larger 2 eV band gap [22] with significant exciton binding [103] (between 0.4-0.83 eV). However, it is well understood that approximate semi-local functionals such as PBE suffer from a systematic band gap problem [104] that may also adversely affect the metal-insulator critical strains. Nevertheless, it is important to emphasize that band alignments and rates of change are quite often reliably reproduced [105], as are the direct-indirect transitions [13] in two-dimensional materials. While absolute band gaps are therefore not expected to be exactly reproduced, we can expect reasonable agreement with trends in electronic and mechanical behavior [106, 107]. The application of uniaxial in-plane strain is found to open the band gap for tensile strain and diminish it for compressive one, while

shear strain has a negligible effect. The electron and hole effective masses (Figs. 2b & 2c), compare well to the figures computed in Ref. [108], where, at $\varepsilon_{xx} = +5\%$ tensile strain, the electron and hole effective masses coincide at $0.9 m_0$ as higher energy bands fall below the conduction band. For compressive strains, the hole effective mass along $\Gamma - X$ rises significantly as the valence band flattens.

Bilayer P is also found to have a direct band gap of 0.43 eV (Fig. 2d) in the relaxed state, and broadly the same behavior as the monolayer, in which case the band gap closes at around -5% uniaxial compressive strain with a predicted Dirac state at the Γ -point. The effect of SOC on the band structure (Fig. 5a) induces no qualitative difference and the three-dimensional bands plotted about the Dirac points (Fig. 5b) confirm the linear-dispersion, albeit in only one direction. A linear fit to the surface of the bands (Fig. 5c) returns a maximum charge velocity of $v = 3.80(1) \times 10^6 \text{ ms}^{-1}$ along $\Gamma - Y$, while, in the orthogonal direction, the bands are flat with a charge velocity that is relatively negligible. This high anisotropy in charge velocities, dominated by ballistic conduction along $\Gamma - Y$, is indicative of effective one-dimensional conductivity and is further supported by the large disparity in effective masses at $\varepsilon_{xx} = -5\%$, evident in Figs. 2e & 2f. The same analysis for $\varepsilon_{yy} = -5\%$, for which the Dirac states are due to band inversion and consequently occur off the $\Gamma - Y$ symmetry line at a point X' , can be found in Figs. 5a - 5c. Here the maximum charge velocity is $v = 3.22(1) \times 10^6 \text{ ms}^{-1}$. These results are further supported by the work of Doh *et al.* [54], who demonstrated the effect of strain on hopping parameters can lead to a Dirac semi-metallic state in bilayer P. Similarly, Baik *et al.* [71] found that the SOC did not induce a band gap in potassium-doped multi-layer P, but did lift the spin-degeneracy of the Dirac points. A direct-indirect band gap transition is also observed at $+2\%$ uniaxial tensile strain. The effective masses (Figs. 2e & 2f), also exhibit broadly the same behavior as the monolayer, due to band-flattening at $\Gamma - X$ and the falling conduction bands along $\Gamma - Y$, which lead to the charge carrier effective masses along $\Gamma - X$ converging at $+4\%$ strain and an increasing hole effective mass for compressive strains.

In the bulk, however, we find that the band gap is completely closed (Fig. 2g), i.e. that the material is metallic. After investigation, we concluded that this was an effect of the smearing functionality [77] in the relaxation procedure and that it contradicts numerous experiments [109–112] that have measured a direct gap in the range of 0.31-0.36 eV. When relaxed under fixed-occupancy conditions, instead, a band gap of ~ 0.35 eV was produced.

While the PBE gap remains closed in the relaxed state, under uniaxial tensile strain it briefly becomes a single-point semi-metal at +2%. At such strains a possible Weyl state is observed, before a direct gap opens that subsequently transitions to an indirect gap at +3%. Shown in Fig. S10 in the Supplemental Material is the three-dimensional band structure with SOC in which a pair of potential Weyl points occur on an off-symmetry point X' along $\Gamma - X$. Here, the SOC slightly reduces the band gap by ~ 0.05 eV and does not qualitatively affect the overall results. The maximum charge velocity is $v = 2.40(1) \times 10^6$ ms $^{-1}$ for both $\varepsilon_{xx} = -5\%$ and $\varepsilon_{yy} = -5\%$ and occurs along a line parallel to $\Gamma - Y$. Under greater compression this band-inversion may also lead to further Weyl states, which have been experimentally observed at similar pressures [60–62]. Again, shear strain is seen to have a negligible effect on the gap. The electron effective masses are quite responsive to strain (Fig. 2h), where those along $\Gamma - Y$ rise for both tensile strain along ε_{xx} , due to falling conduction bands, and compressive strain along ε_{yy} due to flattening bands along $\Gamma - Y$. The effective masses along $\Gamma - X$ were necessarily not computed once the bands overlapped below +2% strain and the hole effective masses are found to vary with respect to the strain to a slightly lesser extent (Fig. 2i).

To summarize, we predict the onset of Γ -point Dirac states in bilayer P at -5% uniaxial compressive strain, with effective one-dimensional conductivity at $\varepsilon_{xx} = -5\%$, and a direct-indirect band gap transition at +2% tensile strain. We also predict the existence of a possible Weyl states at +2% tensile strain in bulk P, followed by a direct-indirect band gap transition at +3%. Finally, effective masses are found to be particularly responsive to ε_{xx} uniaxial strain.

2. Arsenic

In contrast to P, we identify an indirect band gap of 0.15 eV along the $\Gamma - Y$ direction in the relaxed As monolayer (Fig. 3a), which is significantly lower than the predicted DFT-HSE06 gap [98] of 0.83 eV. However, the relaxed band structure and band gap profiles closely resemble those in Refs. [28, 49]. The band gap diminishes for tensile strain along ε_{xx} and at +2% the material becomes semi-metallic with a Dirac state at the Γ -point emerging at $\varepsilon_{xx} = +5\%$ accompanied by an electron pocket above the Fermi-level (Fig. S11 in the Supplemental Material), which is unaffected by the SOC. The maximum charge velocity here

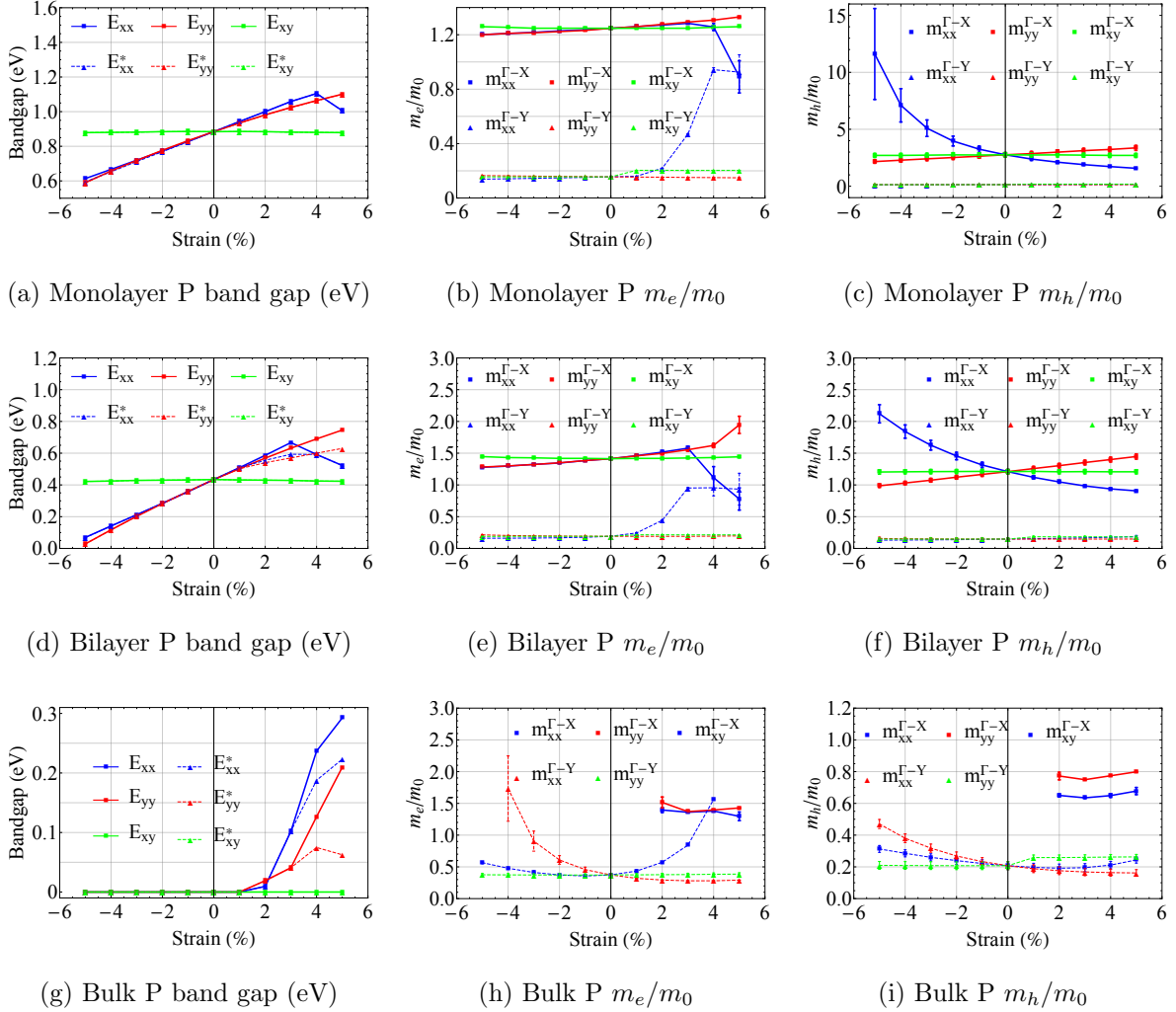


FIG. 2: (Color online) The relationships between the applied in-plane strains ε_{xx} (blue), ε_{yy} (red) and ε_{xy} (green) against [(a), (d), (g)] the direct E (solid squares) and indirect E^* (dashed triangles) band gaps (eV) ; [(b), (e), (h)] the effective electron masses m_e/m_0 along $\Gamma - X$ (solid squares) and $\Gamma - Y$ (dashed triangles) ; [(c), (f), (i)] the effective hole masses m_h/m_0 along $\Gamma - X$ (solid squares) and $\Gamma - Y$ (dashed triangles); for each phase of P.

is $v = 3.01(1) \times 10^6 \text{ ms}^{-1}$ and lies along $\Gamma - Y$. In the orthogonal direction the bands are flat, similarly to monolayer P, with a relatively small charge velocity. This high anisotropy in charge velocities, dominated by the ballistic conduction along $\Gamma - Y$, is again indicative of effective one-dimensional conductivity and is further supported by the large disparity in effective masses at $\varepsilon_{xx} = 5\%$, shown in Figs. 3b & 3c.

For compressive strain along ε_{xx} the indirect band gap closes along $\Gamma - Y$ at $\varepsilon_{xx} = -2\%$.

For tensile strain along ε_{yy} the indirect band gap opens where an indirect-direct transition [28] occurs at $\varepsilon_{xx} = -3\%$. Similar to monolayer phosphorus, there is no appreciable effect due to shear-strain. Meanwhile, the charge-carrier effective masses (Figs. 3b & 3c) respond linearly to uniaxial strain and compare well to other works [101], where, in particular, valence band broadening along $\Gamma - X$ leads to an increasing hole effective mass.

For bilayer As, we identify a direct band gap of 0.45 eV (Fig. 3d), in contrast to the indirect band gap observed in the monolayer. Here, the band gap opens for uniaxial tensile strain and diminishes for compressive strain. The direct band gap transitions to an indirect gap at both $\varepsilon_{yy} = -3\%$ and $\varepsilon_{yy} = +2\%$, while at $\varepsilon_{xx} = +2\%$ it also transitions to an indirect gap before resuming to a direct gap again at $\varepsilon_{xx} = +3\%$. Moreover, we predict a Dirac state at the Γ -point at a compressive strain of $\varepsilon_{xx} = -4\%$ (Fig. S11 in the Supplemental Material) for which the maximum charge velocity is $v = 2.62(2) \times 10^6 \text{ ms}^{-1}$ along $\Gamma - Y$. Along $\Gamma - X$ the bands are also flat, similar to the monolayer, and have a relatively negligible charge velocity. The high anisotropy in charge velocities, is again indicative of effective one-dimensional conductivity, dominated by the ballistic conduction along $\Gamma - Y$, and is further supported by the large disparity in effective masses at $\varepsilon_{xx} = 5\%$, shown in Figs. 3e & 3f. Here again, the SOC has no appreciable effect on the bands. The electron and hole effective masses (Figs. 3e & 3f) respond approximately linearly to the applied strain, where conduction band broadening leads to increased effective electron masses, and valence band flattening at Γ leads to increasing hole effective masses for strain along ε_{yy} .

Finally, no band gap is determined in the relaxed bulk phase (Fig. 3g), again contrary to experiments [113], where a small direct band gap of ~ 0.3 eV is observed. However, at $\varepsilon_{xx} = +1\%$ strain, a potential Weyl state is briefly observed on an off-symmetry point X' (Fig. S12 in the Supplemental Material) before a direct gap opens that subsequently transitions to an indirect one at $\varepsilon_{xx} = +3\%$, after which it reduces again. Another potential Weyl state around the same off-symmetry point X' is also predicted to occur between $+1\% \leq \varepsilon_{yy} \leq +2\%$ after which a direct band gap also appears. The recalculated band structure with the SOC for $\varepsilon_{yy} = +1\%$ (Fig. S12) confirms the linear-dispersion. The maximum charge velocity in both cases occurs along a line parallel to $\Gamma - Y$ and is $v = 1.38(1) \times 10^6 \text{ ms}^{-1}$. Meanwhile, the electron and hole effective masses along $\Gamma - Y$ (Figs. 3h & 3i) increase rapidly for compressive strains as the band peaks rapidly flatten at the Γ -point.

In summary, we predict Γ -point Dirac states in the monolayer and bilayer of As, which

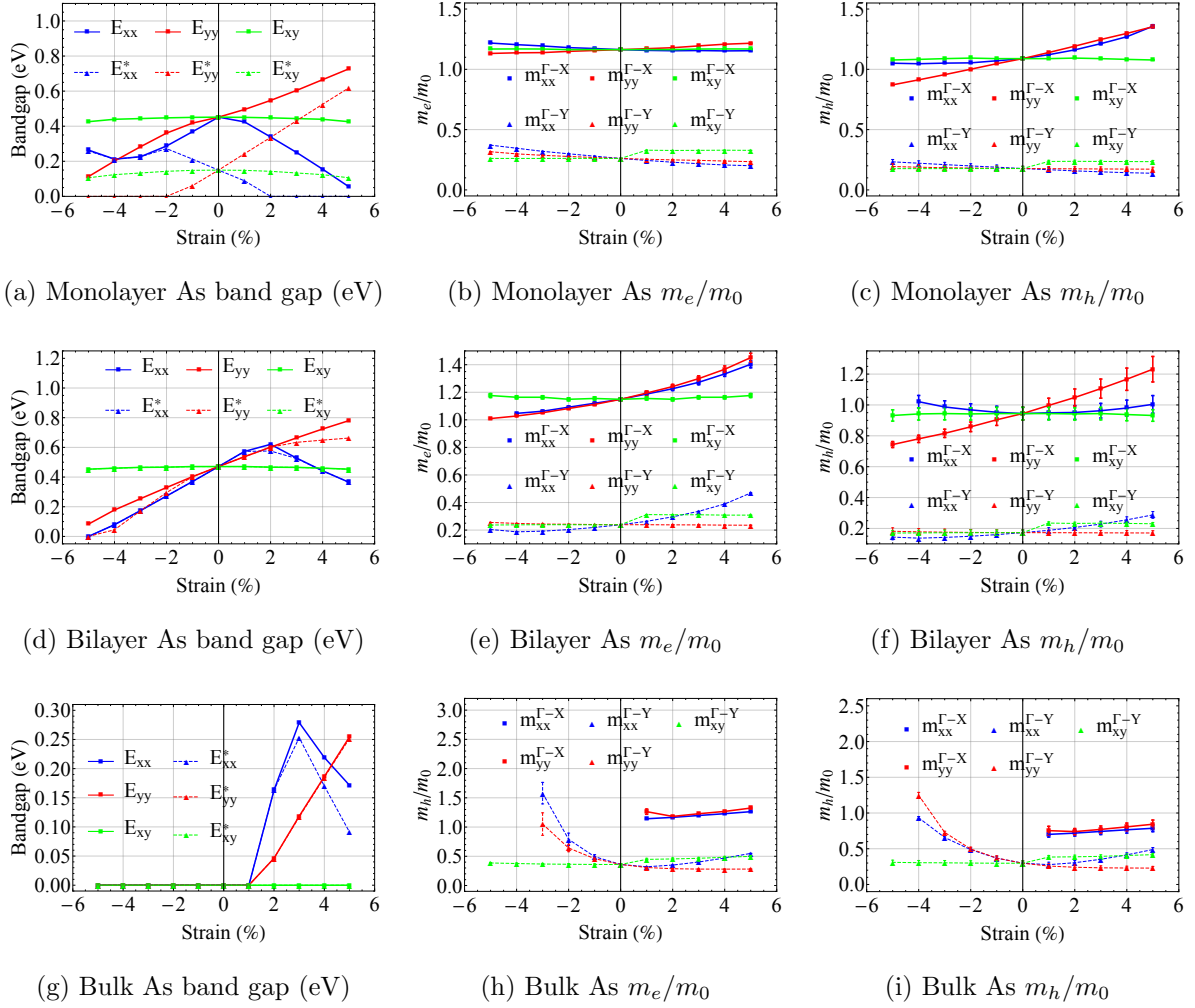


FIG. 3: (Color online) The relationships between the applied in-plane strains ε_{xx} (blue), ε_{yy} (red) and ε_{xy} (green) against [(a), (d), (g)] the direct (solid squares) and indirect (dashed triangles) band gaps (eV); [(b), (e), (h)] the effective electron masses m_e/m_0 along $\Gamma - X$ (solid squares) and $\Gamma - Y$ (dashed triangles); [(c), (f), (i)] the effective hole masses m_h/m_0 along $\Gamma - X$ (solid squares) and $\Gamma - Y$ (dashed triangles); for each phase of As.

support one-dimensional ballistic conduction, as well as possible Weyl states on off-symmetry points in the bulk at moderate levels of in-plane stress that are unaffected by the SOC. We also observe several band gap transitions, in particular in the monolayer phase, which also include semi-conducting-metallic transitions. Finally, the effective masses respond approximately linearly with respect to uniaxial strain, except in the bulk, which exhibits quadratic behavior.

3. Antimony

The relaxed Sb monolayer is found to possess an indirect band gap of 0.21 eV along $\Gamma - Y$ (Fig. 4a), which is reasonably comparable to other PBE values 0.28 [29]-0.37 [114] eV, although these have been obtained by including SOC. For tensile strain along ε_{yy} the band gap opens, suggesting an indirect-direct transition for strains above 6–7%, and it diminishes for compressive strains before finally closing at $\varepsilon_{yy} = -2\%$, where the material becomes a semi-metal. Similarly, the indirect gap closes along $\Gamma - X$ at a compressive strain of $\varepsilon_{xx} = -2\%$ at which monolayer Sb again becomes semi-metallic. The indirect gap transitions to a direct gap at $\varepsilon_{xx} = +1\%$ tensile strain and remains so until finally closing at $\varepsilon_{xx} = +4\%$, at which point we predict a potential Dirac state along $\Gamma - Y$ at an off-symmetry point [37] Y' (Fig. 5g) that has also been predicted in Ref. [51]. Fig. 5g depicts the calculated band structure, in which it is shown that SOC preserves the Dirac state but does not open the band gap. The three-dimensional band structure about the Dirac point is shown in Fig. 5h in which the maximum charge velocity is $v = 4.31(1) \times 10^6 \text{ ms}^{-1}$ and occurs along a line parallel to the $\Gamma - Y$ direction (Fig. 5i). Moreover, the valence band at the X -point undergoes a Rashba splitting [115] due to SOC, which is also predicted to occur in the monolayers of α -P [116], and β -Sb [52, 117]. Finally, the electron effective masses experience a weak linear response to strain (Figs. 4b & 4c), while the hole effective masses along $\Gamma - X$ respond much more strongly to a rapid broadening or flattening of the valence band.

Furthermore, the relaxed bilayer phase is found to be semi-metallic where an indirect band gap opens at $\varepsilon_{yy} = +3\%$ tensile strain and for uniaxial strains $< -1\%$ band-inversion at the Γ -point leads to a fully-metallic state. In addition, a possible Dirac state emerges at a similar non-symmetry-point Y' along $\Gamma - Y$ for $\varepsilon_{xx} = +2\%$ tensile strain (Fig. S13 in the Supplemental Material) and remains in place up to at least $+5\%$ strain. The maximum charge velocity $v = 4.47(3) \times 10^6 \text{ ms}^{-1}$ is also along $\Gamma - Y$ and is approximately the same as that of the monolayer. The effective masses (Figs. 4e & 4f) experience mild linear-response to strains prior to the transition to full metallicity, at which point a rapid flattening of the bands at the Γ -point suggesting strong electron localization. Beyond a compressive strain of $\varepsilon_{yy} = -3\%$, however, at a stress of $\sim 0.3 \text{ GPa}$, the bilayer undergoes a structural transition and buckles in the puckered (\vec{y}) direction. This buckled structure has a total energy 1.7 meV/atom lower than that of the relaxed state of the unperturbed α -bilayer and

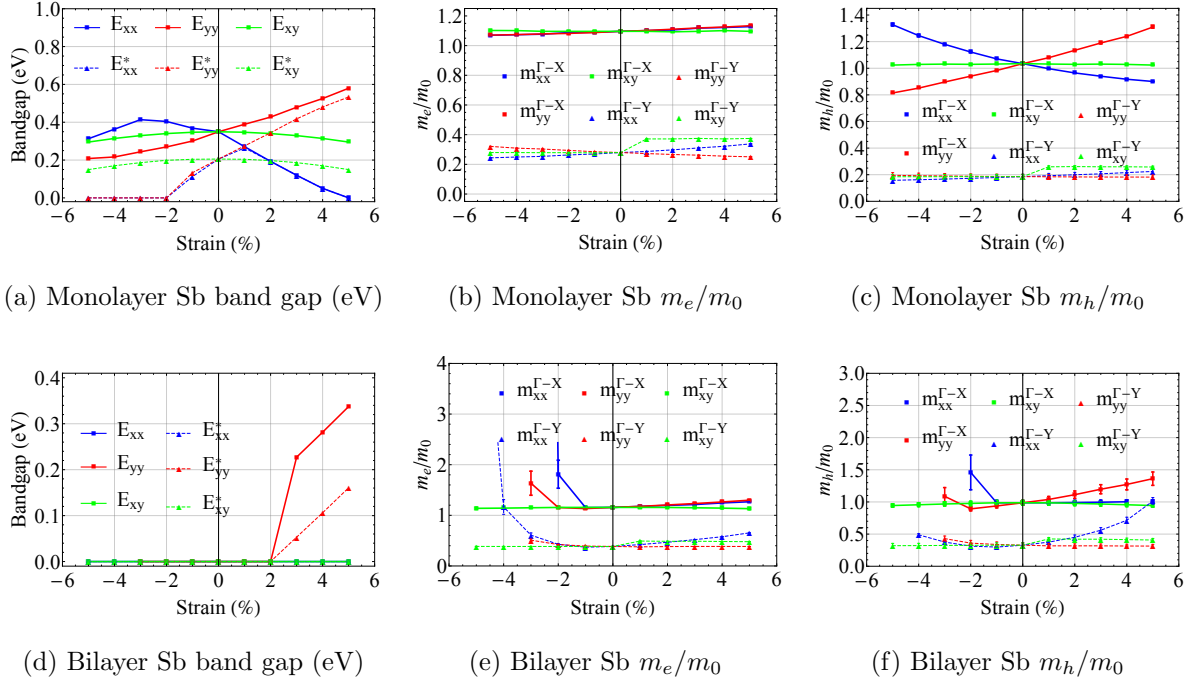


FIG. 4: (Color online) The relationships between the applied in-plane strains ε_{xx} (blue), ε_{yy} (red) and ε_{xy} (green) against [(a), (d), (g)] the direct (solid squares) and indirect (dashed triangles) band gaps (eV) ; [(b), (e), (h)] the effective electron masses m_e/m_0 along $\Gamma - X$ (solid squares) and $\Gamma - Y$ (dashed triangles) ; [(c), (f), (i)] the effective hole masses m_h/m_0 along $\Gamma - X$ (solid squares) and $\Gamma - Y$ (dashed triangles); for each monolayer and bilayer Sb.

3.0 meV/atom lower when allowed to fully-relax, as shown above in Fig. 1c. This suggests the possible existence of a new structure that is attainable via strain.

Finally, bulk Sb is found to be completely metallic for all levels of strain explored in this work. However, shear strains in this case do appear to have a significant effect on the bands despite not opening a gap. In summary, we predict possible non-symmetry-point Dirac states in the strained monolayer and bilayer of Sb, which are qualitatively unaffected by SOC, as well as Rashba splitting at the X -point in the monolayer. We also predict indirect-direct and indirect-semi-metallic transitions in the monolayer phase and a band gap opening in the bilayer phase. Finally, we observe a buckled state induced in bilayer Sb at -4% compressive strain. Bulk Sb was found to be metallic at all levels of strain explored.

In Table II below we present a summary of the calculated band gaps and effective charge

carrier masses for the relaxed phases of each structure, and in Table III we provide a synopsis of the band gap and phase transitions of interest. Finally, in Fig. 5, we present the band structures of bilayer P and monolayer Sb, that form a representative sample of the different Dirac points predicted at Γ , X' and Y' , as well the three-dimensional band structures about the region of the points.

	E_g (eV)	$Me_{\Gamma-X}$	$Me_{\Gamma-Y}$	$Mh_{\Gamma-X}$	$Mh_{\Gamma-Y}$
P _{mono}	0.9	1.25(1)	0.16(1)	2.8(2)	0.14(1)
AS _{mono}	0.15 \star	1.16(1)	0.26(1)	1.09(1)	0.18(2)
Sb _{mono}	0.2 \star	1.10(1)	0.28(1)	1.04(1)	0.19(2)
P _{bi}	0.4	1.41(1)	0.19(1)	1.21(3)	0.15(2)
AS _{bi}	0.45	1.15(1)	0.24(1)	0.94(4)	0.17(2)
Sb _{bi}	0 \dagger	1.16(1)	0.39(1)	0.99(4)	0.33(4)
P _{bulk}	0 \ddagger	-	0.37(2)	-	0.21(2)
AS _{bulk}	0 \ddagger	-	0.36(1)	-	0.30(3)
Sb _{bulk}	0 \ddagger	-	-	-	-

TABLE II: (Color online) Kohn-Sham band gaps (eV), indicating the indirect semiconducting (\star), semi-metallic (\dagger) and metallic (\ddagger) states, as well as the charge-carrier effective masses (m_0) for each phase of P, As, Sb.

C. Isotropic bulk properties

In order to obtain these electronic states, and to ensure accurate strain-engineering, knowledge of the mechanical properties is paramount. Therefore, in this section we review the mechanical response of the few-layer and bulk phases in order to compute the elastic properties, both isotropically averaged and as a function of orientation of applied in-plane stress.

The computed elements of the stiffness tensor C in GPa of each structure are given in Table S1 in the Supplemental Material, where those pertaining to bulk P compare well to experiments [118, 119] and similarly computed values [96, 108]. For the elements related to in-plane strains (c_{11} , c_{22} , c_{66} , c_{12}) we observe an expected increase in stiffness as the layer

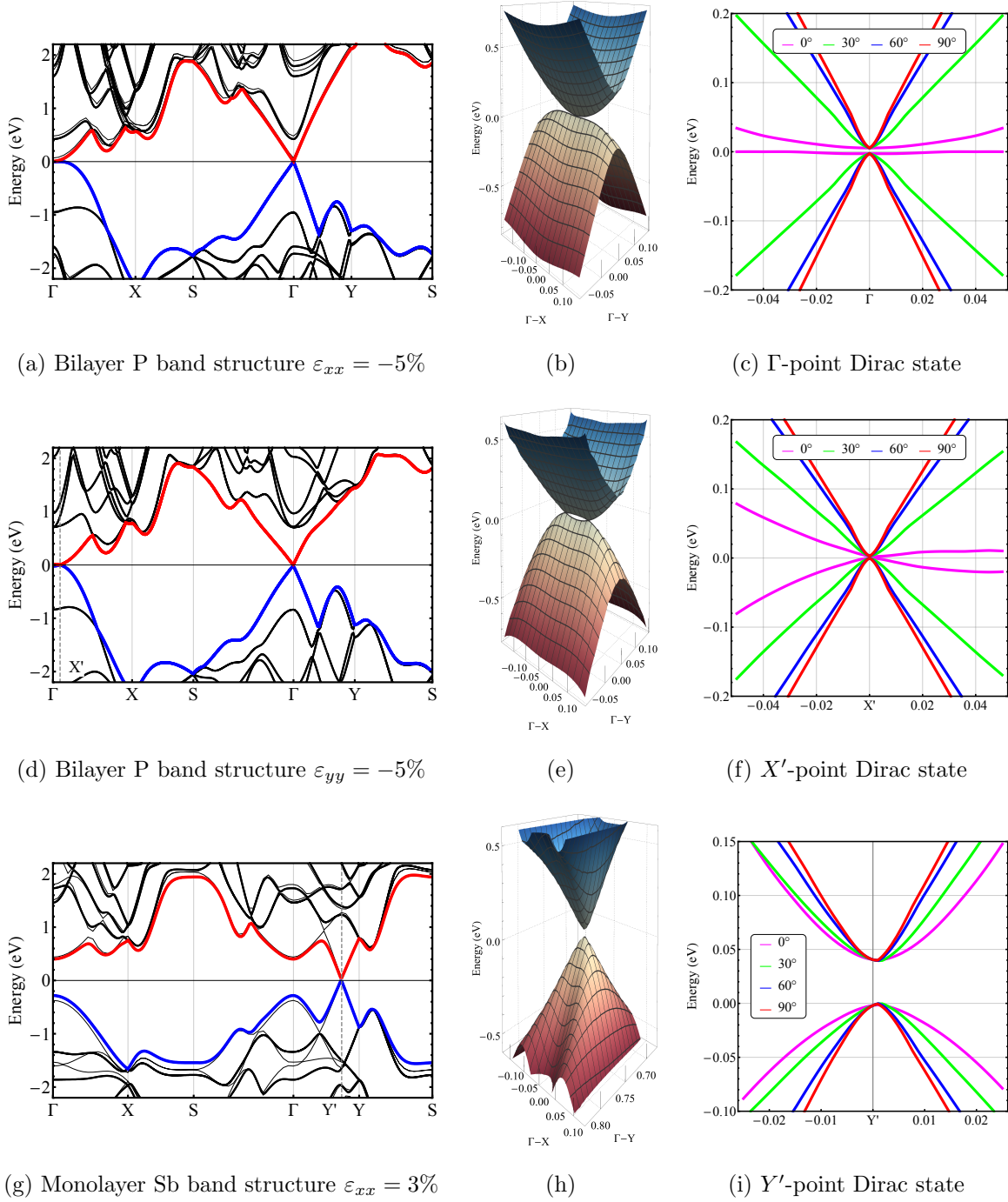


FIG. 5: (Color online) a) Band structure of bilayer P at $\varepsilon_{xx} = -5\%$ with SOC (thick lines), and without SOC (thin lines) b) three-dimensional bands about the predicted Dirac point at Γ c) slices through the Dirac point at 0° , 30° , 60° and 90° relative to the $\Gamma - X$ line that indicate highly anisotropic conduction. [5d,5e,5f] Illustrates the same for bilayer P at $\varepsilon_{yy} = -5\%$, where the Dirac state occurs at the non-symmetry point X' along $\Gamma - X$. [5g,5h,5i] Illustrates the same for monolayer Sb at $\varepsilon_{xx} = 3\%$, where the possible Dirac state occurs at the non-symmetry point Y' along $\Gamma - Y$.

	Transition	Direction	Strain (%)
P_{bi}	D Gap \rightarrow SM $^{\Delta}$	XX,YY	-5
	D Gap \rightarrow ID Gap	XX,YY	+2
P_{bulk}	SM \rightarrow D Gap \rightarrow ID Gap	XX,YY	+1 \rightarrow +3
	SM \rightarrow SM $^{\nabla}$	XX,YY	+2
As_{mono}	ID \rightarrow D Gap	XX	-3
	ID Gap \rightarrow SM	XX	+2
	ID Gap \rightarrow SM	XX	+2
	SM \rightarrow SM $^{\Delta}$	XX	+5
As_{bi}	D Gap \rightarrow ID Gap \rightarrow D Gap	XX	+2 \rightarrow +3
	D Gap \rightarrow ID Gap	YY	-3,+2
As_{bulk}	SM \rightarrow D Gap \rightarrow ID Gap	XX	0 \rightarrow +3
	SM \rightarrow D Gap	YY	0 \rightarrow +3
	SM \rightarrow SM $^{\nabla}$	XX,YY	+1
Sb_{mono}	ID Gap \rightarrow SM	XX	-2
	ID Gap \rightarrow D Gap \rightarrow SM $^{\Delta}$	XX	+2 \rightarrow +4
	ID Gap \rightarrow SM	YY	-2
Sb_{bi}	SM \rightarrow SM $^{\Delta}$	XX	+4
	Structural Transition	YY	-3
	SM \rightarrow ID Gap	YY	+3

TABLE III: Summary of the band gap transitions including direct (D); indirect (ID); metallic (M); and semi-metallic (SM), in particular those that indicate potential Dirac states (Δ), Weyl states (∇), and the structural phase transition.

number increases and for increasing atomic number. However, for other elements relating to out-of-plane and shear stresses (c_{33} , c_{44} , c_{55} , c_{23} , c_{13}) the stiffness actually increases in the bulk phase from P to As to Sb.

The Hill-averaged bulk properties are presented in Table IV, which compare well to other DFT values [96, 108], while our calculated bulk modulus for bulk P (37.2 GPa) is also within reasonable range of the experimental values (32.32 [100] - 36.02 GPa [120]). We also observe

	Y_H (GPa)	G_H (GPa)	ν_H	\mathcal{B}_H (GPa)
P _{bulk}	61.1 (70.3 ^a)	24.9 (29.4 ^a)	0.23 (0.30 ^a)	37.2 (38.5 ^a , 32.32 ^b , 36.02 ^c)
As _{bulk}	60.0	23.8	0.26	41.4
Sb _{bulk}	52.5	21.1	0.24	33.8

^a Ref. [96]

^b Ref. [100]

^c Ref. [120]

TABLE IV: The Hill-averaged Young’s modulus Y_H , shear modulus G_H and bulk modulus \mathcal{B} in GPa, and Poisson’s ratio ν_H for bulk P, As and Sb compared to similarly calculated DFT [96] values and available experimental data [100, 120].

that the bulk properties remain largely comparable for all the species, but generally decrease from P to As to Sb (except for the Poisson’s ratio and bulk modulus, which are largest for As). We also note that while bulk P has the largest in-plane responses, As and Sb have larger out-of-plane and shear responses, which enable the net isotropic properties for all the species to remain comparable overall.

D. In-plane elastic properties

In section S1 of the Supplemental Material we re-derive the equations for the elastic properties as a function of the in-plane orientation angle θ , defined in Fig. 1, as outlined in Ref. [121]. These functions are the plotted in Fig. 6 and include the Young’s modulus $Y(\theta)$ and its average $\langle Y(\theta) \rangle$, the shear modulus $G(\theta)$, and Poisson’s ratio $\nu(\theta)$. The experimental Young’s modulus of 130 GPa, determined in Ref. [11] via the ROM of a nano-flake-polymer composite, lies precisely between the average in-plane bulk Young’s modulus 85.7 GPa and the elastic stiffness in the zigzag (\vec{x}) direction 187.9 GPa, thus fitting the results of our model reasonably well.

The anisotropy of the elastic properties is also apparent in the mechanical profiles, particularly with regard to the Young’s modulus, which has a 2-fold symmetry about the x -axis, in contrast to the shear modulus and Poisson’s ratios, which display 4-fold symmetry about both the axes (except for the Poisson’s ratio of P, which remains 2-fold symmetric). Indeed,

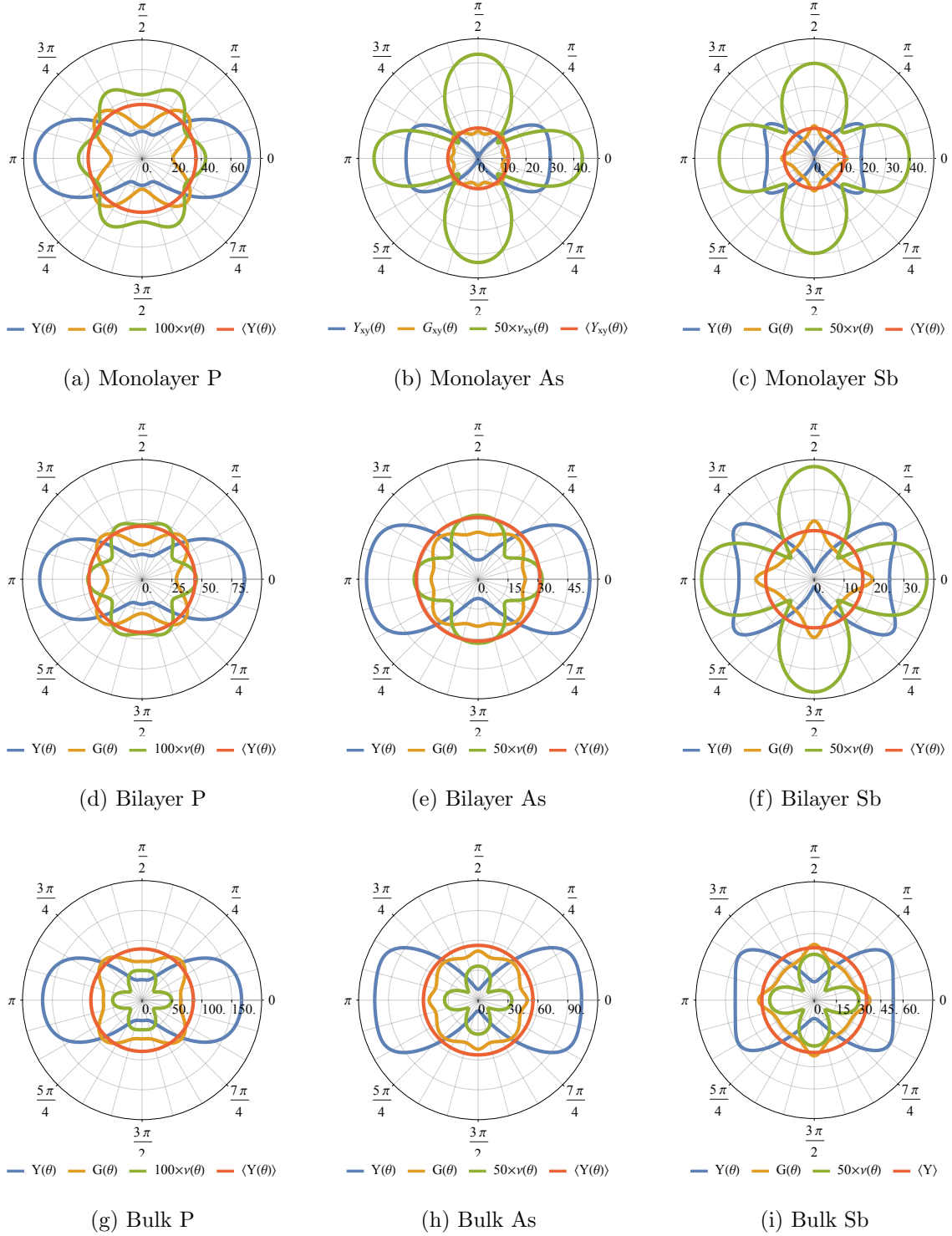


FIG. 6: (Color online) In-plane functions for the Young's modulus $Y(\theta)$ (blue) and its isotropic average $\langle Y(\theta) \rangle$ (red) in units of GPa; shear modulus $G(\theta)$ in GPa (orange); and Poisson's ratio $\nu(\theta)$ (green, scaled by 100 for P and 50 for As, Sb) for each of the structures.

	Y_{\min}	θ	Y_{\max}	θ	$\langle Y \rangle$	G_{\min}	θ	G_{\max}	θ	$\langle G \rangle$	ν_{\min}	θ	ν_{\max}	θ	$\langle \nu \rangle$
P _{mono}	17.1	69°	72.4	0°	36.4	20.9	90°	42.2	45°	31.0	0.3	31°	0.5	63°	0.5
As _{mono}	-2.1	90°	30.5	18°	12.7	10.4	77°	13.8	45°	11.2	0.2	39°	0.9	90°	0.4
Sb _{mono}	1.4	90°	24.4	22°	12.6	8.9	45°	13.6	90°	9.4	0.3	43°	0.8	90°	0.6
Pb _{bi}	20.5	75°	85.6	0°	44.4	28.1	90°	49.2	45°	37.8	0.31	34°	0.5	68°	0.4
As _{bi}	9.7	90°	56.0	0°	31.0	23.0	78°	28.6	45°	24.3	0.4	40°	0.6	90°	0.5
Sb _{bi}	2.6	90°	31.6	33°	16.3	11.8	45°	19.5	90°	12.8	0.2	42°	0.8	90°	0.5
P _{bulk}	34.2	87°	166.4	0°	85.7	64.9	87°	92.4	45°	74.5	0.2	36°	0.5	75°	0.3
As _{bulk}	10.9	90°	105.1	20°	55.0	44.4	73°	51.1	45°	66.7	0.3	40°	0.7	90°	0.4
Sb _{bulk}	12.4	90°	58.9	30°	35.4	28.1	59°	28.2	45°	63.2	0.2	41°	0.6	90°	0.4

TABLE V: Summary of the minima and maxima of the Hill-averaged in-plane Young’s modulus $Y(\theta)$ (GPa), shear modulus $G(\theta)$ (GPa), and Poisson’s ratio $\nu(\theta)$ as well as the angle θ with respect to the \vec{x} -direction (zigzag) at which they occur in degrees, and their in-plane averages.

for a given species, the general shape of each profile is approximately preserved with respect to the number of layers, while the range of each property tends to increase. This discovery is advantageous in the strain-engineering of nano-flakes since one may now forecast in advance the response of a material to in-plane strain, once the underlying profile and number of layers are known.

Another interesting feature is that the extrema of the elastic functions do not necessarily coincide with the coordinate-axes. For instance the Young’s modulus maximum for monolayer Sb occurs at 22°. Table V summarizes the global minima and maxima of each function and the angles at which they occur. While most of the function extrema occur expectedly at 0°, 45° or 90°, many are incident away from the coordinate-axes. This result lends further insight into the mechanical anisotropy of the orthorhombic group- V materials.

The emergence of a negative Young’s modulus of -2.1 GPa in monolayer As (Fig. 6b), at first glance, may give cause for concern. It arises due to a negative Voigt estimate for the Young’s modulus at 90° where $(c_{22}^2 - c_{12}^2)/c_{22} = -8.9$ GPa (since $c_{12} > c_{22}$), which is larger in absolute magnitude than the Reuss estimate at 90° given by $1/s_{22} = 4.7$ GPa and results

in a net negative Hill-average. In this instance, we surmise that either the assumptions of the Voigt model break down, or the Hill-method is not universally appropriate in arbitrary directions in-plane and a more robust averaging scheme must be employed. Nevertheless, the qualitative in-plane functions and their isotropic averages remain physically meaningful and in general can provide valuable physical insight.

In contrast to the isotropic averages for the bulk properties in Table IV, which remained largely comparable for P, As and Sb, a much clearer trend across the species emerges once we have eliminated contributions from the out-of-plane and shear stresses. In this instance, P clearly possesses superior in-plane mechanical strength in both moduli, which decrease with the number of layers as expected As and Sb are largely similar in the monolayer, though less so in the bilayer and bulk phases, where they are stronger in the \vec{x} -direction. In contrast, the Poisson's ratio tends to remain relatively stable aside from generally decreasing with increasing number of layers.

In summary, there exists in the elastic properties a broad range of responses, profile shapes and behavior that is reflective of the underlying anisotropic crystal structure, which also strongly depend on the number of layers with P typically the stiffest and Sb the most flexible. In general we find the shapes of the in-plane response profiles to be conveniently consistent, which implies that, for a given number of layers, the in-plane elastic response of a nano-flake can be reliably estimated *a priori*.

IV. CONCLUSION

We have extensively explored the mechanical and electronic properties of P, As and Sb in their few-layer and bulk phases. We have identified several band gap transitions in almost all of the structures. The SOC tended to close the bands by ~ 0.05 eV but did not alter any of our qualitative findings. We also predict the existence of Dirac states in the strained phases of monolayer As and Sb, bilayer P, As and Sb as well as possible Weyl states in bulk P and As for moderate levels of strain. The linear-dispersion was observed along $\Gamma - Y$ of each of the predicted Dirac or Weyl states, corresponding to the direction of softest mechanical response in the puckered direction. The maximum charge velocity is calculated to be over 10^6 ms⁻¹. In particular, for bilayer P and few-layer As we predict highly anisotropic conductivity dominated by ballistic transport along the puckered direction that is indicative of effective,

one-dimensional conduction. We predict that an appropriate strain could yield these effects in experiments.

We also observe the existence of a notable buckled state of compressed bilayer Sb at -4% strain. Finally, the angular-resolved elastic properties as well as the stress-dependence of the Kohn-Shame band gaps and charge-carrier effective masses revealed highly anisotropic behavior, spanning a broad range of values, and angular-dependent behavior that has become characteristic of these group-V layered structures. Moreover, the critical stresses at which these transitions occur are expected to be experimentally accessible and highly switchable, paving the way for possible verification in the near future. Thus, the group-V layered materials are poised to become central to the next generation of electronic devices with potential novel applications in field-effect transistors; batteries; gas-sensors and opto-electronic devices.

ACKNOWLEDGMENTS

The authors would like to sincerely thank Damien Hanlon, Claudia Backes, Conor Boland, Jonathan Coleman, Beata Szydłowska, Gaozhong Wang, and Werner Blau for their helpful discussions relating to the work conducted for this Article. This work was enabled by Science Foundation Ireland (SFI) funded centre AMBER (SFI/12/RC/2278). All calculations were performed on the Kelvin cluster maintained by Trinity College Dublin Research IT and funded through grants from SFI.

-
- [1] M. Wu, H. Fu, L. Zhou, K. Yao, and X. C. Zeng, *Nano Lett.* **15**, 3557 (2015).
 - [2] J. Guan, Z. Zhu, and D. Tománek, *Phys. Rev. Lett.* **113**, 046804 (2014).
 - [3] Z. Zhu and D. Tománek, *Phys. Rev. Lett.* **112**, 176802 (2014).
 - [4] J. Guan, Z. Zhu, and D. Tomnek, *ACS Nano* **8**, 12763 (2014).
 - [5] L. Li, Y. Yu, G. J. Ye, Q. Ge, X. Ou, H. Wu, D. Feng, X. H. Chen, and Y. Zhang, *Nat. Nano* **9**, 372 (2014).
 - [6] F. Xia, H. Wang, and Y. Jia, *Nat. Commun.* **5**, 4458 EP (2014).
 - [7] S. P. Koenig, R. A. Doganov, H. Schmidt, A. H. C. Neto, and B. Ozyilmaz, *Appl. Phys. Lett.* **104**, 103106 (2014).

- [8] H. Liu, A. T. Neal, Z. Zhu, Z. Luo, X. Xu, D. Tomnek, and P. D. Ye, *ACS Nano* **8**, 4033 (2014).
- [9] X. Ling, H. Wang, S. Huang, F. Xia, and M. S. Dresselhaus, *Proc. Natl. Acad. Sci. U.S.A.* **112**, 4523 (2015).
- [10] J. R. Brent, N. Savjani, E. A. Lewis, S. J. Haigh, D. J. Lewis, and P. O'Brien, *Chem. Commun.* **50**, 13338 (2014).
- [11] D. Hanlon, C. Backes, E. Doherty, C. S. Cucinotta, N. C. Berner, C. Boland, K. Lee, A. Harvey, P. Lynch, Z. Gholamvand, S. Zhang, K. Wang, G. Moynihan, A. Pokle, Q. M. Ramasse, N. McEvoy, W. J. Blau, J. Wang, G. Abellan, F. Hauke, A. Hirsch, S. Sanvito, D. D. O'Regan, G. S. Duesberg, V. Nicolosi, and J. N. Coleman, *Nat. Commun.* **6**, 8563 (2015).
- [12] A. S. Rodin, A. Carvalho, and A. H. Castro Neto, *Phys. Rev. Lett.* **112**, 176801 (2014).
- [13] X. Peng, Q. Wei, and A. Copple, *Phys. Rev. B* **90**, 085402 (2014).
- [14] J.-W. Jiang and H. S. Park, *Phys. Rev. B* **91**, 235118 (2015).
- [15] B. Sa, Y.-L. Li, J. Qi, R. Ahuja, and Z. Sun, *J. Phys. Chem. C* **118**, 26560 (2014).
- [16] M. Elahi, K. Khaliji, S. M. Tabatabaei, M. Pourfath, and R. Asgari, *Phys. Rev. B* **91**, 115412 (2015).
- [17] T. Hu, Y. Han, and J. Dong, *Nanotechnology* **25**, 455703 (2014).
- [18] J.-W. Jiang and H. S. Park, *Nat. Commun.* **5**, 4727 EP (2014).
- [19] R. Fei and L. Yang, *Nano Lett.* **14**, 2884 (2014).
- [20] H. Liu, Y. Du, Y. Deng, and P. D. Ye, *Chem. Soc. Rev.* **44**, 2732 (2015).
- [21] J. Qiao, X. Kong, Z.-X. Hu, F. Yang, and W. Ji, *Nat. Commun.* **5**, 4475 EP (2014).
- [22] V. Tran, R. Soklaski, Y. Liang, and L. Yang, *Phys. Rev. B* **89**, 235319 (2014).
- [23] R. W. Keyes, *Phys. Rev.* **92**, 580 (1953).
- [24] Q. Wei and X. Peng, *Appl. Phys. Lett.* **104**, 251915 (2014).
- [25] C. Yongqing, Z. Gang, and Z. Yong-Wei, *Sci. Rep.* , 1 (2014).
- [26] A. C.-G. Zant, L. Vicarelli, E. Prada, J. O. Island, K. L. Narasimha-Acharya, S. I. Blanter, D. J. Groenendijk, M. Buscema, G. A. Steele, J. V. Alvarez, H. W. Zandbergen, J. J. Palacios, and H. S. J. van der, *2D Mater.* **1**, 025001 (2014).
- [27] K. Momma and F. Izumi, *J. Appl. Crystallogr.* **44**, 1272 (2011).
- [28] C. Kamal and M. Ezawa, *Phys. Rev. B* **91**, 085423 (2015).
- [29] G. Wang, R. Pandey, and S. P. Karna, *ACS Appl. Mater. Inter.* **7**, 11490 (2015).

- [30] I. Kokubo, Y. Yoshiike, K. Nakatsuji, and H. Hirayama, [Phys. Rev. B **91**, 075429 \(2015\)](#).
- [31] Y. Lu, W. Xu, M. Zeng, G. Yao, L. Shen, M. Yang, Z. Luo, F. Pan, K. Wu, T. Das, P. He, J. Jiang, J. Martin, Y. P. Feng, H. Lin, and X.-s. Wang, [Nano Lett. **15**, 80 \(2015\)](#).
- [32] Z. Zhu, J. Guan, and D. Tomnek, [Nano Lett. **15**, 6042 \(2015\)](#).
- [33] F. Shojaei and H. S. Kang, [J. Phys. Chem. C **119**, 20210 \(2015\)](#).
- [34] M. Xie, S. Zhang, B. Cai, Y. Huang, Y. Zou, B. Guo, Y. Gu, and H. Zeng, [Nano Energy **28**, 433 \(2016\)](#).
- [35] B. Liu, M. Kpf, A. N. Abbas, X. Wang, Q. Guo, Y. Jia, F. Xia, R. Wehrich, F. Bachhuber, F. Pielhofer, H. Wang, R. Dhall, S. B. Cronin, M. Ge, X. Fang, T. Nilges, and C. Zhou, [Adv. Mater **27**, 4423 \(2015\)](#).
- [36] L. Kou, Y. Ma, X. Tan, T. Frauenheim, A. Du, and S. Smith, [J. Phys. Chem. C **119**, 6918 \(2015\)](#).
- [37] V. Pardo and W. E. Pickett, [Phys. Rev. Lett. **102**, 166803 \(2009\)](#).
- [38] C. Shekhar, A. K. Nayak, Y. Sun, M. Schmidt, M. Nicklas, I. Leermakers, U. Zeitler, Y. Skourski, J. Wosnitza, Z. Liu, Y. Chen, W. Schnelle, H. Borrmann, Y. Grin, C. Felser, and B. Yan, [Nat Phys **11**, 645 \(2015\)](#), letter.
- [39] X. Wan, A. M. Turner, A. Vishwanath, and S. Y. Savrasov, [Phys. Rev. B **83**, 205101 \(2011\)](#).
- [40] H. Nielsen and M. Ninomiya, [Phys. Lett. B **130**, 389 \(1983\)](#).
- [41] A. M. Turner, A. Vishwanath, and C. O. Head, [Topological Insulators **6**, 293 \(2013\)](#).
- [42] S. A. Parameswaran, T. Grover, D. A. Abanin, D. A. Pesin, and A. Vishwanath, [Phys. Rev. X **4**, 031035 \(2014\)](#).
- [43] S. M. Young, S. Zaheer, J. C. Y. Teo, C. L. Kane, E. J. Mele, and A. M. Rappe, [Phys. Rev. Lett. **108**, 140405 \(2012\)](#).
- [44] Z. Wang, Y. Sun, X.-Q. Chen, C. Franchini, G. Xu, H. Weng, X. Dai, and Z. Fang, [Phys. Rev. B **85**, 195320 \(2012\)](#).
- [45] Z. Wang, H. Weng, Q. Wu, X. Dai, and Z. Fang, [Phys. Rev. B **88**, 125427 \(2013\)](#).
- [46] Z. Liu, J. Wang, and J. Li, [Phys. Chem. Chem. Phys. **15**, 18855 \(2013\)](#).
- [47] J. Wang, S. Deng, Z. Liu, and Z. Liu, [Nat. Sci. Rev. **2**, 22 \(2015\)](#).
- [48] J. Kim, S. S. Baik, S. H. Ryu, Y. Sohn, S. Park, B.-G. Park, J. Denlinger, Y. Yi, H. J. Choi, and K. S. Kim, [Science **349**, 723 \(2015\)](#).
- [49] C. Wang, Q. Xia, Y. Nie, M. Rahman, and G. Guo, [AIP Advances **6**, 035204 \(2016\)](#).

- [50] G. Yao, Z. Luo, F. Pan, W. Xu, Y. P. Feng, and X.-s. Wang, *Sci. Rep.* **3**, 2010 EP (2013).
- [51] Y. Lu, D. Zhou, G. Chang, S. Guan, W. Chen, Y. Jiang, J. Jiang, X.-s. Wang, S. A. Yang, Y. P. Feng, Y. Kawazoe, and H. Lin, *NPJ Comput. Mater.* **2**, 16011 EP (2016).
- [52] M. Zhao, X. Zhang, and L. Li, *Sci Rep* **5**, 16108 (2015).
- [53] S. Zhang, M. Xie, B. Cai, H. Zhang, Y. Ma, Z. Chen, Z. Zhu, Z. Hu, and H. Zeng, *Phys. Rev. B* **93**, 245303 (2016).
- [54] H. Doh and H. J. Choi, *2D Mater.* **4**, 025071 (2017).
- [55] S. Zhang, Z. Yan, Y. Li, Z. Chen, and H. Zeng, *Angew. Chem. Int. Ed.* **54**, 3112 (2015).
- [56] A. Manjanath, A. Samanta, T. Pandey, and A. K. Singh, *Nanotechnology* **26**, 075701 (2015).
- [57] J. Han, J. Xie, Z. Zhang, D. Yang, M. Si, and D. Xue, *Appl. Phys. Express* **8**, 041801 (2015).
- [58] Z. Zhu, J. Guan, and D. Tománek, *Phys. Rev. B* **91**, 161404 (2015).
- [59] T. Hu and J. Dong, *Phys. Rev. B* **92**, 064114 (2015).
- [60] Z. J. Xiang, G. J. Ye, C. Shang, B. Lei, N. Z. Wang, K. S. Yang, D. Y. Liu, F. B. Meng, X. G. Luo, L. J. Zou, Z. Sun, Y. Zhang, and X. H. Chen, *Phys. Rev. Lett.* **115**, 186403 (2015).
- [61] P.-L. Gong, D.-Y. Liu, K.-S. Yang, Z.-J. Xiang, X.-H. Chen, Z. Zeng, S.-Q. Shen, and L.-J. Zou, *Phys. Rev. B* **93**, 195434 (2016).
- [62] R. Fei, V. Tran, and L. Yang, *Phys. Rev. B* **91**, 195319 (2015).
- [63] A. N. Abbas, B. Liu, L. Chen, Y. Ma, S. Cong, N. Aroonyadet, M. Kpf, T. Nilges, and C. Zhou, *ACS Nano* **9**, 5618 (2015).
- [64] L. Kou, T. Frauenheim, and C. Chen, *J. Phys. Chem. Lett.* **5**, 2675 (2014).
- [65] T. Low, A. S. Rodin, A. Carvalho, Y. Jiang, H. Wang, F. Xia, and A. H. Castro Neto, *Phys. Rev. B* **90**, 075434 (2014).
- [66] M. Baba, Y. Takeda, K. Shibata, T. Ikeda, and A. Morita, *Jpn. J. Appl. Phys.* **28**, L2104 (1989).
- [67] C.-M. Park and H.-J. Sohn, *Adv. Mater* **19**, 2465 (2007).
- [68] L.-Q. Sun, M.-J. Li, K. Sun, S.-H. Yu, R.-S. Wang, and H.-M. Xie, *J. Phys. Chem. C* **116**, 14772 (2012).
- [69] J. Sun, H.-W. Lee, M. Pasta, H. Yuan, G. Zheng, Y. Sun, Y. Li, and Y. Cui, *Nat. Nano* **10**, 980 (2015).

- [70] J. Sun, G. Zheng, H.-W. Lee, N. Liu, H. Wang, H. Yao, W. Yang, and Y. Cui, [Nano Lett.](#) **14**, 4573 (2014).
- [71] S. S. Baik, K. S. Kim, Y. Yi, and H. J. Choi, [Nano Lett.](#) **15**, 7788 (2015).
- [72] P. Giannozzi, S. Baroni, N. Bonini, M. Calandra, R. Car, C. Cavazzoni, D. Ceresoli, G. L. Chiarotti, M. Cococcioni, I. Dabo, A. D. Corso, S. de Gironcoli, S. Fabris, G. Fratesi, R. Gebauer, U. Gerstmann, C. Gougoussis, A. Kokalj, M. Lazzeri, L. Martin-Samos, N. Marzari, F. Mauri, R. Mazzarello, S. Paolini, A. Pasquarello, L. Paulatto, C. Sbraccia, S. Scandolo, G. Sclauzero, A. P. Seitsonen, A. Smogunov, P. Umari, and R. M. Wentzcovitch, [J. Phys.: Condens. Mat.](#) **21**, 395502 (2009).
- [73] J. P. Perdew, K. Burke, and M. Ernzerhof, [Phys. Rev. Lett.](#) **77**, 3865 (1996).
- [74] D. Vanderbilt, [Phys. Rev. B](#) **41**, 7892 (1990).
- [75] E. Kucukbenli, M. Monni, B. Adetunji, X. Ge, G. Adebayo, N. Marzari, S. De Gironcoli, and A. D. Corso, arXiv preprint arXiv:1404.3015 (2014).
- [76] S. Grimme, [J. Comput. Chem.](#) **27**, 1787 (2006).
- [77] N. Marzari, D. Vanderbilt, A. De Vita, and M. C. Payne, [Phys. Rev. Lett.](#) **82**, 3296 (1999).
- [78] V. Iyer, P. Ye, and X. Xu, [2D Mater.](#) **4**, 021032 (2017).
- [79] C. R. Dean, F. A. Young, I. Meric, C. Lee, L. Wang, S. Sorgenfrei, K. Watanabe, T. Taniguchi, P. Kim, K. L. Shepard, and J. Hone, [Nat. Nano](#) **5**, 722 (2010).
- [80] K.-K. Liu, W. Zhang, Y.-H. Lee, Y.-C. Lin, M.-T. Chang, C.-Y. Su, C.-S. Chang, H. Li, Y. Shi, H. Zhang, C.-S. Lai, and L.-J. Li, [Nano Lett.](#) **12**, 1538 (2012).
- [81] J. C. H. Affdl and J. L. Kardos, [Polym. Eng. Sci.](#) **16**, 344 (1976).
- [82] R. Mullen, R. Ballarini, Y. Yin, and A. Heuer, [Acta Mater.](#) **45**, 2247 (1997).
- [83] R. Hearmon, *Physics of the Solid State*, 401 (1969).
- [84] J. M. J. den Toonder, J. A. W. van Dommelen, and F. P. T. Baaijens, [Model. Simul. Mater. Sc.](#) **7**, 909 (1999).
- [85] A. Reuss, [ZAMM-Z Angew. Math. Mech.](#) **9**, 49 (1929).
- [86] R. D. Cook and W. C. Young, *Advanced Mechanics of Materials* (Pearson College Division, 1999).
- [87] W. Voigt, [Ann. Phys.](#) **274**, 573 (1889).
- [88] R. Hill, [P. Phys. Soc.](#) **65**, 349 (1952).

- [89] U. Khan, P. May, A. O'Neill, A. P. Bell, E. Boussac, A. Martin, J. Semple, and J. N. Coleman, [Nanoscale](#) **5**, 581587 (2013).
- [90] W. E. Mahmoud, [Eur. Polym. J.](#) **47**, 1534 (2011).
- [91] J. Liang, Y. Huang, L. Zhang, Y. Wang, Y. Ma, T. Guo, and Y. Chen, [Adv. Funct. Mater.](#) **19**, 2297 (2009).
- [92] J. A. King, D. R. Klimek, I. Miskioglu, and G. M. Odegard, [J. Appl. Polym. Sci.](#) **128**, 4217 (2013).
- [93] R. J. Young, I. A. Kinloch, L. Gong, and K. S. Novoselov, [Compos. Sci. Technol.](#) **72**, 1459 (2012).
- [94] Y. Yang, W. Rigdon, X. Huang, and X. Li, [Sci. Rep.](#) **3**, 2086 EP (2013).
- [95] S.-K. Kim, J. J. Wie, Q. Mahmood, and H. S. Park, [Nanoscale](#) **6**, 7430 (2014).
- [96] S. Appalakondaiah, G. Vaitheeswaran, S. Lebègue, N. E. Christensen, and A. Svane, [Phys. Rev. B](#) **86**, 035105 (2012).
- [97] D. Kecik, E. Durgun, and S. Ciraci, [Phys. Rev. B](#) **94**, 205410 (2016).
- [98] Z. Zhang, J. Xie, D. Yang, Y. Wang, M. Si, and D. Xue, [Appl. Phys. Express](#) **8**, 055201 (2015).
- [99] Y. Xu, B. Peng, H. Zhang, H. Shao, R. Zhang, and H. Zhu, [Ann. Phys.](#) **529**, 1600152 (2017).
- [100] L. Cartz, S. R. Srinivasa, R. J. Riedner, J. D. Jorgensen, and T. G. Worlton, [J. Chem. Phys.](#) **71**, 1718 (1979).
- [101] P. M. Smith, A. J. Leadbetter, and A. J. Apling, [Philos. Mag.](#) **31**, 57 (1975).
- [102] C. S. Barrett, P. Cucka, and K. Haefner, [Acta Crystallogr.](#) **16**, 451 (1963).
- [103] D. Çakır, H. Sahin, and F. m. c. M. Peeters, [Phys. Rev. B](#) **90**, 205421 (2014).
- [104] A. J. Cohen, P. Mori-Sánchez, and W. Yang, [Phys. Rev. B](#) **77**, 115123 (2008).
- [105] Y. Hinuma, A. Grüneis, G. Kresse, and F. Oba, [Phys. Rev. B](#) **90**, 155405 (2014).
- [106] U. von Barth, [Phys. Scripta](#) **2004**, 9 (2004).
- [107] A. J. Cohen, P. Mori-Sánchez, and W. Yang, [Chem. Rev.](#) **112**, 289 (2012).
- [108] Y. Wang and Y. Ding, [Nanoscale Res. Lett.](#) **10**, 254 (2015).
- [109] A. Morita, [Appl. Phys. A](#) **39**, 227 (1986).
- [110] D. Warschauer, [J. Appl. Phys.](#) **34**, 1853 (1963).
- [111] S. Narita, Y. Akahama, Y. Tsukiyama, K. Muro, S. Mori, S. Endo, M. Taniguchi, M. Seki, S. Suga, A. Mikuni, and H. Kanzaki, [Physica B&C](#) **117**, 422 (1983).

- [112] Y. Maruyama, S. Suzuki, K. Kobayashi, and S. Tanuma, *Physica B&C* **105**, 99 (1981).
- [113] G. Greaves, S. Elliott, and E. Davis, *Adv. Phys.* **28**, 49 (1979).
- [114] O. U. Aktürk, V. O. Özçelik, and S. Ciraci, *Phys. Rev. B* **91**, 235446 (2015).
- [115] G. Bihlmayer, O. Rader, and R. Winkler, *New J. Phys.* **17**, 050202 (2015).
- [116] Z. S. Popović, J. M. Kurdestany, and S. Satpathy, *Phys. Rev. B* **92**, 035135 (2015).
- [117] L. Yang, Y. Song, W. Mi, and X. Wang, *RSC Adv.* **6**, 66140 (2016).
- [118] M. Yoshizawa, I. Shirotnani, and T. Fujimura, *J. Phys. Soc. Jpn.* **55**, 1196 (1986).
- [119] Y. Kzuki, Y. Hanayama, M. Kimura, T. Nishitake, and S. Endo, *J. Phys. Soc. Jpn.* **60**, 1612 (1991).
- [120] T. Akai, S. Endo, Y. Akahama, K. Koto, and Y. Marljyama, *High Pressure Res.* **1**, 115 (1989).
- [121] R. M. Jones, *Mechanics of Composite Materials*, Vol. 193 (Scripta Book Company Washington, DC, 1975).